

# Efficient atomistic simulations of radiation damage in W and W-Mo using machine-learning potentials

Mikko Koskenniemi,<sup>1,\*</sup> Jesper Byggmästar,<sup>1</sup> Kai Nordlund,<sup>1</sup> and Flyura Djurabekova<sup>1,2</sup>

<sup>1</sup>*Department of Physics, P.O. Box 43, FI-00014 University of Helsinki, Finland*

<sup>2</sup>*Helsinki Institute of Physics, Helsinki, Finland*

(Dated: August 2, 2022)

The Gaussian approximation potential (GAP) is an accurate machine-learning interatomic potential that was recently extended to include the description of radiation effects. In this study, we seek to validate a faster version of GAP, known as tabulated GAP (tabGAP), by modelling primary radiation damage in 50-50 W-Mo alloys and pure W using classical molecular dynamics. We find that W-Mo exhibits a similar number of surviving defects as in pure W. We also observe W-Mo to possess both more efficient recombination of defects produced during the initial phase of the cascades, and in some cases, unlike pure W, recombination of all defects after the cascades cooled down. Furthermore, we observe that the tabGAP is two orders of magnitude faster than GAP, but produces a comparable number of surviving defects and cluster sizes. A small difference is noted in the fraction of interstitials that are bound into clusters.

## I. INTRODUCTION

Nuclear energy is an integral part of modern society; nuclear fuels are millions of times more energy-dense than chemical ones, such as oil. Moreover, they release no greenhouse gases. The materials in nuclear reactors are exposed to intense irradiation, and the understanding of the consequences of this process on the durability and reliability of the materials is vital not only for existing power plants but more so for future fusion and next-generation fission reactors [1]. This motivates the search for new radiation-tolerant materials. Tungsten-based high-entropy alloys (HEA) are a class of materials that show promising resilience to radiation [2], making them particularly interesting in the field of nuclear energy applications.

Molecular dynamics [3] (MD) is a widely used method to study how materials respond to radiation and gives insight into atomic-scale phenomena and their underlying mechanisms that are inaccessible by experimental means [4]. Considering specifically W-based alloys, Qiu et al. [5] found, by running collision-cascade simulations, that alloying Ta with W can decrease the size of dislocation loops, whilst retaining comparable defect production to W. Moreover, cascade simulations have shown Mo-based complex concentrated alloys to fare well under radiation [6]. However, the effects of collision cascades in W-based alloys are still fairly poorly understood.

Interatomic potentials that describe the nature of atom interactions within the modelled material are essential for the validity and accuracy of simulation results. However, analytical potentials (potentials that have a fixed mathematical form, comprising only a few parameters) struggle to accurately describe more than a handful of phenomena, fundamentally restricting the use of their applications. Recently, a new approach to the development of interatomic potentials based on machine-learning (ML) algorithms was proposed [7, 8].

Since the training database is generated from consistent density functional theory (DFT) calculations, some of the ML potentials excel at describing a multitude of different phenomena, giving more accurate results than their analytical counterparts [7–9].

The Gaussian approximation potential (GAP) [7] is a popular machine-learning potential, which has been proven to give results that are on par with quantum-mechanical simulation methods, and is capable of successfully describing a diverse range of phenomena [10, 11]. GAP also reaps the benefits of classical potentials, being capable of simulating systems that are at least thousands of times larger than in quantum-mechanical methods. Despite this, GAP is still excruciatingly slow when put up against its traditional, analytical counterparts, such as the embedded atom method (EAM) potentials. In an attempt to retain the excellent array of properties of GAP, whilst making it faster to compute, the tabulated GAP (tabGAP) formalism was created [12, 13].

The key feature of tabGAP is using only low-dimensional descriptor terms, omitting terms like the *Smooth Overlap of Atomic Positions (SOAP)* term [14], which is a vector in a space of hundreds or even thousands of dimensions for multi-component materials. The low-dimensional terms enable tabGAP to circumvent the exhausting machine-learning prediction of GAP when computing atomic energies by using tabulation. Tabulation involves pre-computing the GAP energy predictions and mapping them onto low-dimensional grids. After tabulation, the resulting data grid can be used in conventional spline interpolation methods during simulations, which makes tabGAP faster. Perhaps even more importantly, the low-dimensional terms of tabGAP make it easier to develop for many-element materials like HEAs because they need less training data than terms like SOAP [13]. Therefore, tabGAP could act as a gateway to efficient, and accurate, studies of exotic multi-component materials.

\* Corresponding author, mikko.a.koskenniemi@gmail.com

In the present study, we test the tabGAP developed

in Ref. [12], which was developed for a W-based HEA, namely molybdenum-niobium-tantalum-vanadium-tungsten (Mo-Nb-Ta-V-W), by modelling radiation effects. To compare the performance of tabGAP to other types of interatomic potentials in MD simulations, we choose to model 50-50 Mo-W alloys. We note that the high activation of Mo under neutron irradiation limits the use of this particular alloy for fusion applications; however, it could be used in small amounts e.g. in fusion reactor diagnostics, and in non-fusion applications where neutron activation is not an issue. Our choice is motivated by the existence of both a GAP and EAM for W-Mo [15, 16]. Additionally, the results of this study give general insight into how 50-50 W-based refractory alloys behave. Radiation damage in both 50-50 W-Mo alloys and pure W is modelled by the means of MD collision-cascade simulations using tabGAP, a SOAP-equipped GAP, and EAM. The simulation results are analysed for the number of surviving defects: point defects and their clusters.

## II. METHODS

### A. Software and potentials

The simulations were run using the classical MD code, *Large-scale Atomic/Molecular Massively Parallel Simulator* (LAMMPS) [17] (<https://www.lammps.org/>). The QUIP code [7] (<https://github.com/libAtoms/QUIP>) was used to enable the use of GAP with LAMMPS. The *Open Visualization Tool* [18] (OVITO) was used for both visualising simulation results and defect analysis using the Wigner-Seitz method. Dislocations were analysed using the *Dislocation Extraction Algorithm* [19]. The Python library Matplotlib [20] was used for plotting simulation data.

Cascades were run using four potentials: the EAM potential developed for W-Mo in Ref. [16] (hereafter referred to as *W-Mo-EAM*), the Ackland-Thetford-Zhong-Nordlund (AT-ZN) EAM potential developed for W in Ref. [21, 22], the GAP developed in Ref. [15], and the tabGAP developed in Ref. [12]. We chose the AT-ZN potential for pure W, for it is the most widely used potential for radiation damage simulations in W [23, 24]. For example, it has shown good agreement with experiments and GAP at high doses [24], which makes a comparison to the other potentials useful.

All four potentials were developed to be applicable for the simulation of radiation effects, i.e. joined with corresponding repulsive potentials, such as the ZBL potential in EAM [25] and DMol [26] in GAP and tabGAP, to enable a reasonable description of cascade development.

### B. Selection of the primary knock-on atom

Following the practice in [26], cascades were initiated by giving one atom, the primary knock-on atom (PKA), a recoil of a given energy towards the centre of the simulation cell. The PKAs were selected as follows. Firstly, we generate a random direction in three-dimensional space. Then, we define a point at a specific distance from the centre of the cell, in the aforementioned direction. Finally, the atom closest to this point is given the recoil in the aforementioned direction, towards the cell centre, to initiate the cascade.

Higher recoil energies trigger more extensive cascades, hence the distance at which a PKA was selected, as well as the total number of atoms in the simulation cell, scale up with the recoil energy. These parameters are given in Table I. For consistency, all PKA positions, energies and directions were used identically in all potentials for a given material.

It is worth noting that because the PKAs were selected in random directions, they may move in channelling directions (which offer the least resistance to movement), a few cascades overlapped with the periodic boundaries, in spite of the sufficient size of the simulation cells. These simulations were discarded and the simulations were re-run with new PKAs. The aim of the PKA selection method is to minimise the direction-related bias in the results. Regardless, the present results are not completely free of directional bias, since the channelling directions were excluded from the analysis. However, the main purpose of the current paper, which is to compare the results of different interaction models, is unaffected by this, since the probability of crossing the boundaries is the same for all interaction models.

TABLE I: Simulation parameters. Here,  $E_{\text{PKA}}$  is the initial kinetic energy of a PKA,  $r_{\text{PKA}}$  is the distance from the PKA to the centre of the lattice, and  $n_{\text{atoms}}$  is the number of atoms in the lattice.

$E_{\text{PKA}}$ (keV)	$r_{\text{PKA}}$ (Å)	$n_{\text{atoms}}$
1	15	31 250
2	15	54 000
5	20	159 014
10	30	332 750
20	40	686 000

### C. Simulation setup

Collision cascade simulations were run for 50-50 W-Mo alloys, and pure W, both with the body-centred cubic (BCC) lattice structure. The atoms in the W-Mo alloys are randomly ordered. Periodic boundary conditions were used in every simulation.

In W-Mo alloys, the cascades initiated by PKA with energies from 1 to 20 keV were run using the EAM and

tabGAP potentials, but only 1 to 5-keV cascades were run using GAP, due to its much higher computational cost. In pure W, simulations were run using the W-part of the W-Mo-EAM potential and of the tabGAP to study stable defects and their clusters with PKA energies of 1 to 10 keV. Only 1-keV cascade simulations were run in pure W with the GAP; 5 and 10 keV were run using the AT-ZN EAM. For each PKA energy, statistics were collected over 40 simulations with different initial seeds for random-number generation, except for GAP 5 keV in W-Mo. In the latter case, only 25 simulations were run, again due to the prohibitively high power requirements of these simulations.

For consistency, in all applied potentials, we used cells of the same composition. Therefore, we relaxed the simulation cells with the corresponding potential before cascade simulations. The relaxation was done by imposing a Nosé-Hoover thermostat and barostat to the cells [27, 28], and waiting for the pressure and volume of the cells to become stable. Cascade simulations started out at a temperature of 300 K, and had a Nosé-Hoover thermostat applied to a 6-Å thick shell at the boundary of the simulation cells, to cool the cell down to its initial temperature, which mimics the much larger bulk material surrounding the cascade region. During the cascade simulations, no pressure control was used. The simulation time was chosen such that the final temperature is sufficiently close to the initial 300 K and the cascade-induced defect evolution has stopped. For each W-Mo simulation, it was 100 ps, with the exception of 5-keV GAP simulations, where the shortest simulation managed to run for about 71 ps. The shorter run-time was deemed a non-issue, as will be discussed in more detail in section III A. For pure W, a shorter simulation time of 60 ps was sufficient.

Due to the nature of the cascade simulations, the initial high kinetic energies of atoms (high velocities) decrease over time. For simulation efficiency, an adaptive time step [29] was used. The magnitude of the adaptive time step changes dynamically in response to atomic velocities, starting out small and ultimately reaching a fixed maximum value, which was chosen to be 3 fs.

In the MD simulations, electrons are not explicitly modelled, however, they do have a substantial role in energy dissipation for the collision energies involved in the cascades of this study [30]. To emulate the energy loss brought about by electronic excitations in collisions, electronic stopping data were used to determine the magnitude of the stopping power that the atoms experience at a given kinetic energy. A cut-off kinetic-energy threshold of 10 eV was used, and the electronic stopping was applied to all atoms with kinetic energy higher than this. The stopping-power data for W-Mo were generated using the SRIM-2013 code [31, 32]. For W, the stopping data were the same as in earlier work [23], generated with the ZBL-96 code [25]. Both stopping-powers are at low energies based on the Lindhard stopping [33], and hence the differences between them are minor.

In addition to the cascade simulations, the mobility of interstitials was determined using tabGAP in both pure W, and 50-50 W-Mo cells. The simulation cells

consisted of 2 000 non-defect atoms and had 5–6 split-interstitials injected into them. No thermostat or barostat was used. A single W simulation was run at 600 K, and one W-Mo simulation at both 600 K and 1200 K, all of which were run for 1 ns using a 3 fs time step.

#### D. Cluster analysis

After a cascade, any given two defects in the simulation cell were considered to belong to the same cluster if they were separated by a chosen cut-off distance. The definitions of the cut-off radii for interstitial and vacancy clusters are the same as in Ref. [34]; for interstitial clusters, the cut-off radius is  $(r_{3NN} + r_{4NN}) / 2$ , and for vacancy clusters  $(r_{2NN} + r_{3NN}) / 2$ , where the distance to the  $k$ th nearest neighbour is  $r_{kNN}$ . The cut-off radii depend on the lattice constant of the cell, which for W-Mo was set to 3.1738 Å, as the lattice constants yielded by all three potentials differed from this by less than 1 %. For pure W, the lattice constant at 300 K given by tabGAP is 3.1892 Å, W-Mo-EAM 3.1714 Å, and AT-ZN EAM 3.1659 Å.

### III. RESULTS AND DISCUSSION

#### A. Defect formation and mobility

In the cascades, all interstitials produced in both W-Mo and W were split-interstitials, i.e. one interstitial comprises two atoms surrounding a lattice site. The interstitials produced in a 10-keV cascade simulation in W-Mo are shown in Fig. 1. One can see single split-interstitials and smaller clusters, where the split-interstitials are mainly parallel to one another.

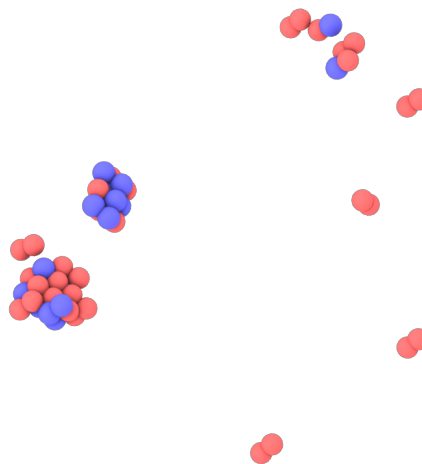


FIG. 1: Interstitials at the end of a cascade simulation in W-Mo. Here the blue atoms are W, and the red atoms are Mo.

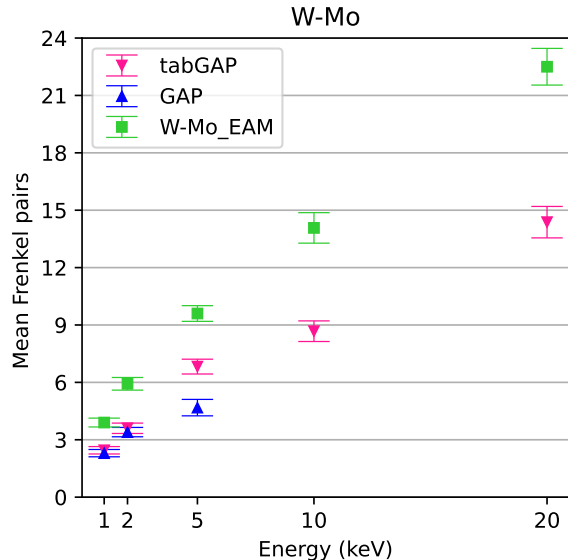
The mean number of Frenkel pairs as a function of the PKA energy is presented in Fig. 2 for both materials. It should be noted that the results of all simulations were included when evaluating averages and standard errors related to the number of defects, even those that ended with no defects. Information on how the results in individual simulations are distributed around the mean is illustrated in Fig. 3.

As shown in Fig. 2, tabGAP and GAP produce a comparable number of defects. At 5 keV in W-Mo, however, tabGAP produces slightly more defects, though given the standard error, the difference can be as low as about 1 to 2 defects. The W-Mo-EAM, on the other hand, produces significantly more defects across the board, in both W-Mo and W. This is likely due to the threshold displacement energies reported in Ref. [16] being too low for the present W-Mo-EAM, although results were only reported for pure Mo. We also observe that the AT-ZN EAM and tabGAP yielded similar defect production, although the mean value of survived defects is slightly higher for tabGAP.

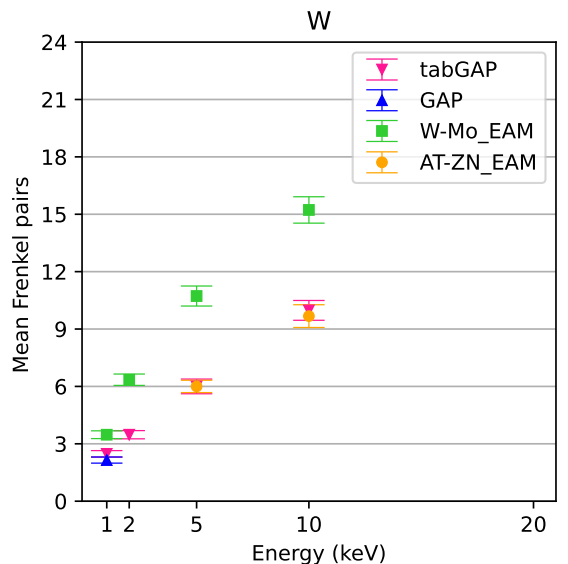
An interesting property of W-Mo manifests itself in the violin plots (Figs. 3a, 3c, and 3e), namely exhibiting recombination of all defects to some extent at lower PKA energies; even in one W-Mo-EAM 1-keV simulation, the cell completely recovered from the damage after the cascade had cooled down. In W, defect recombination was not observed in any of the tested PKA energies, though looking at Fig. 2, tabGAP and GAP describe W as producing roughly the same number of defects as W-Mo (given the standard errors), whereas W-Mo-EAM predicts a greater mean number of defects in W than W-Mo.

In Fig. 4, one can discern the temporal evolution of temperature and defect formation in 5-keV W-Mo and W cascade simulations. We note that the temperature during the highly non-equilibrium peak of the cascade is not a conventional equilibrium temperature, but a measure of the average kinetic energy  $E_{\text{kin}}$  of the system transformed to temperature  $T$  using  $E_{\text{kin}} = \frac{3}{2}Nk_{\text{B}}T$ . The absolute value of the temperature is not meaningful, as it depends on the number of atoms  $N$  in the simulation cell. However, the time dependence of  $T$  is a good illustration of the duration of the non-equilibrium phase of a collision cascade.

On the account of Fig. 4, it is apparent that defects stop being produced shortly after the initial spike in temperature, caused by the development of the cascade. W-Mo demonstrates more efficient recombination of defects produced during the initial phase of the cascades than W; W-Mo has an initial spike of around 130 defects, whereas W has around 100 defects, yet both materials end up with roughly the same mean number of defects. Furthermore, the temperature is removed from the W-Mo cell more efficiently by the W-Mo-EAM potential compared to GAP and tabGAP, both of which had similar predictions. This is apparent from the comparison of the temperature evolution in the simulation cell after the active cascade phase under the same boundary conditions in all three potentials. This dis-



(a)



(b)

FIG. 2: Mean number of Frenkel pairs with respect to PKA energy for cascades in (a) W-Mo and (b) pure W. The vertical bars indicate the standard error. Results from all simulations, even those that ended with zero defects, were included in the averages and the errors thereof.

crepancy may be explained not only by different lattice thermal conductivities but also by cascade size and shape.

The analysis of the interstitial-mobility simulations revealed that interstitials at a given temperature in W-Mo are far less mobile than in W, where interstitials had effectively no movement even at 600 K. At a tempera-

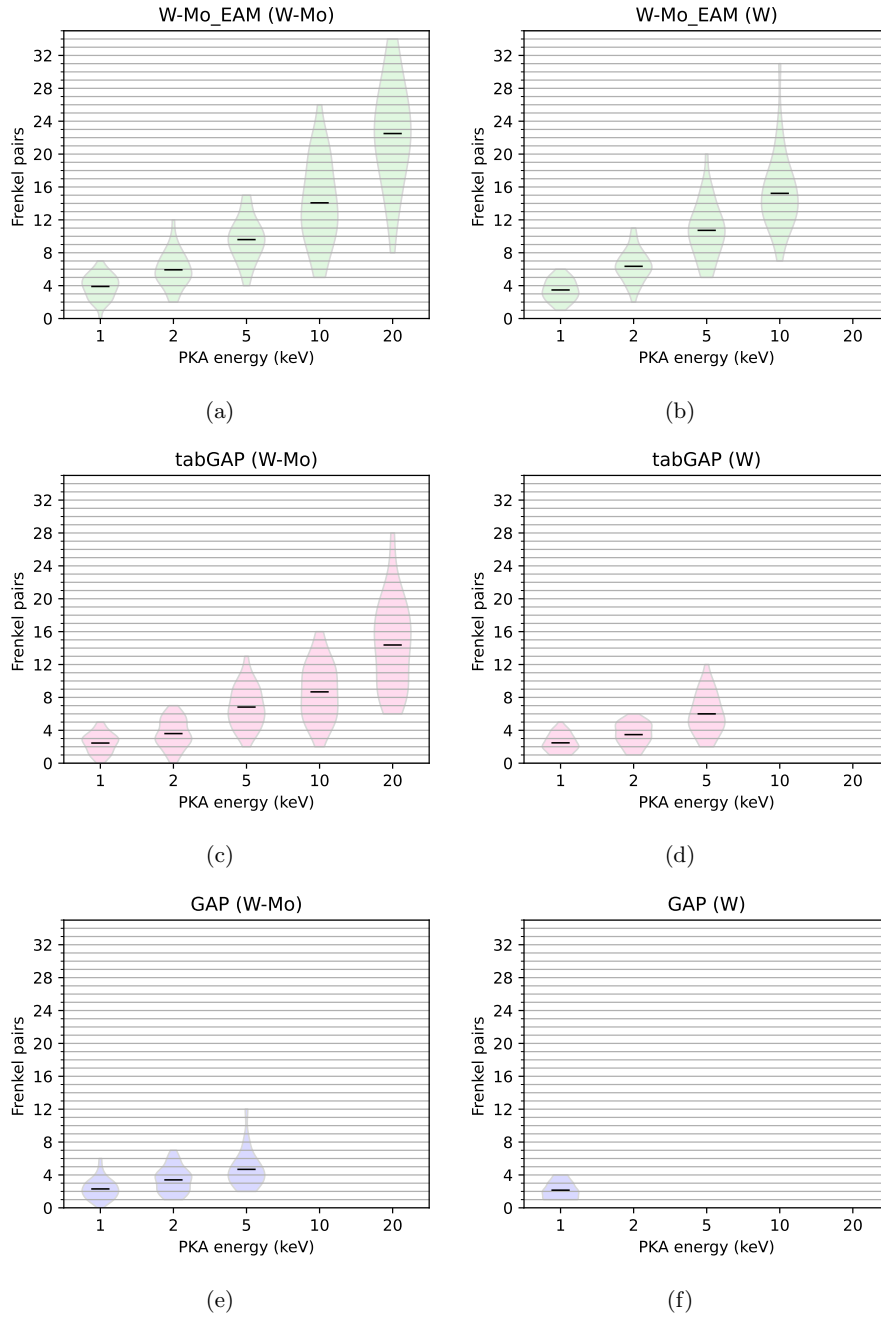


FIG. 3: Frenkel-pair violin plots. W-Mo\_EAM refers to the EAM developed for W-Mo. The horizontal grid in the plots indicates the possible values of the number of Frenkel pairs, the shaded area is the corresponding probability distribution (the wider the area at a given grid-line, the more simulations ended with the number of Frenkel pairs indicated by the line), and the horizontal line inside the violin plots is the mean. All simulation results, even those that ended with no defects, are included in the evaluation of the mean.

ture of 1200 K, the mobility W-Mo interstitials rivalled the mobility pure-W interstitials had at 600 K. The interstitials were observed to migrate mainly in a crowdion  $\langle 111 \rangle$  direction in both W-Mo and W.

Considering that interstitials in W-Mo at 600 K are practically immobile on the MD time scale, and that the temperature even at 5 keV drops far below 600 K during the first few picoseconds, the shorter run-time of GAP 5 keV (shortest was 71 ps) most likely had no effect on defect formation and clustering. In pure W, the temperature was observed to decrease faster than in W-Mo, having reached 300 K long before 60 ps had transpired in 5-keV simulations, as indicated in Fig. 4. This indicates that the lattice thermal conductivity is significantly higher in pure W than in random W-Mo alloys.

### B. Defect clustering

The Mo concentrations in interstitial clusters of 5-keV simulations are depicted in Fig. 5, wherein Mo-Mo is shown to be the predominant type of split-interstitial. Moreover, tabGAP clusters have a slightly larger fraction of W than GAP.

We note that the present tabGAP was trained for Mo-Nb-Ta-V-W, which means a smaller fraction of its training data describes W-Mo interactions than the GAP, which was trained directly for W-Mo alloys. Nevertheless, all three potentials agree that Mo atoms are predominant in interstitial clusters in W-Mo.

Statistical distributions of vacancy and interstitial clusters are shown in Fig. 6. More distributions for the remaining tested energies are given in the Supplementary material. Given the standard errors, the comparison between the different potentials is satisfactory. Some of the clusters are seen in some potentials, but not in others. Overall, the GAP predicts smaller cluster sizes than the W-Mo-EAM and tabGAP, whilst the W-Mo-EAM potential forms cluster more readily than the other tested potentials.

Fig. 6 shows that in pure W, interstitial clusters are more prevalent than in W-Mo, which is reasonable given the increased mobility that interstitials in W have over those in W-Mo. Differences between W-Mo and W in the clustering of interstitials at PKA energies lower than 5 keV are less consistent. This is due to the overall low probability of the formation of large clusters at these energies, which makes the data noisier and less statistically reliable.

The interstitial clustering in W is similar in both tabGAP and AT-ZN EAM, taking into account the margins of error. However, W-Mo-EAM predicts that the vacancies cluster more in pure W than in W-Mo, whereas tabGAP predicts the opposite. Moreover, the AT-ZN EAM predicts a higher number of vacancy clusters (size  $> 1$ ) than tabGAP.

We note that TabGAP's prediction of more efficient clustering of vacancies in W-Mo is more likely to be correct than the W-Mo-EAM potential. This is be-

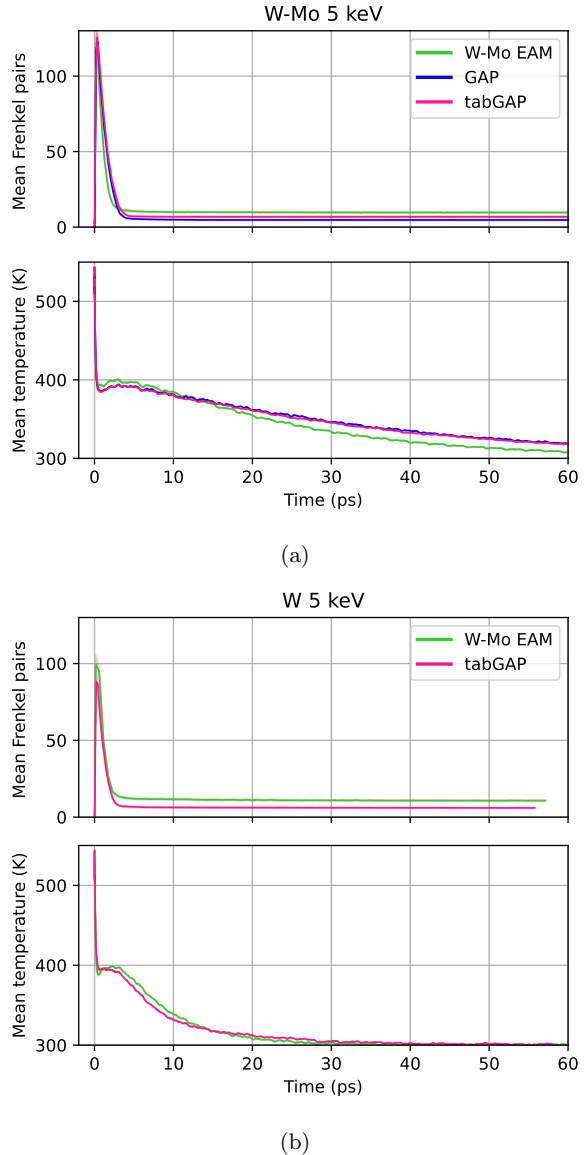


FIG. 4: Mean defect-formation and temperature plots for W-Mo and W 5-keV simulations. The top plots show the mean number of Frenkel pairs, and the bottom plots show the mean temperature, both with respect to time. Standard error, albeit very small, is represented by a shaded red area. The x-axis (time) is shared among the defect and temperature plots. The x-axis has been limited to 60 ps for clarity. Results from all simulations, even those that ended with zero defects, were included in the averages and the errors thereof.

cause, unlike most metals, small vacancy clusters in W tend to be energetically unstable [35] (more than in pure Mo [36]). This trend is known to be poorly reproduced by classical EAM potentials, whilst GAP is able to capture this feature better [9, 36]. Moreover, in the 1-keV simulations (plots given in the Supplemen-

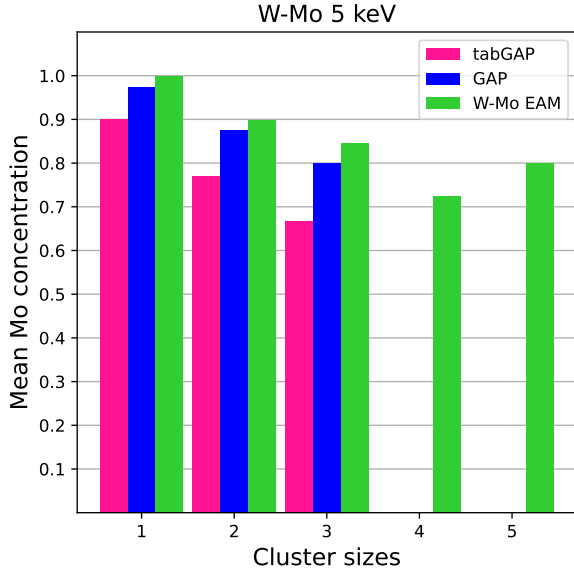


FIG. 5: Average fraction of Mo found in interstitial clusters in 5 keV simulations, with respect to cluster size. W-Mo EAM is the EAM developed for W-Mo. Size-1 clusters are single split-interstitials, comprising two atoms.

tary material), GAP and tabGAP both produce fewer vacancy clusters (with similar distributions) in pure W than W-Mo-EAM. It is, therefore, reasonable to assume that alloying W with Mo increases the stability of small vacancy clusters, and that both GAP and tabGAP reproduce this trend as they are (partially) trained to the same data.

The clustered fraction of defects is a quantity that allows us to analyse the clustering efficiency of the formed defects in a given potential. It is evaluated as follows:

$$\frac{N_{\text{tot}} - N_c}{N_{\text{tot}}}, \quad (1)$$

where  $N_c$  is the number of defects, vacancies or interstitials, bound into clusters with size greater than 1, and  $N_{\text{tot}}$  is the total number of defects of the corresponding type. This quantity is shown for W-Mo and W in Fig. 7.

The cases with zero defects are excluded from this analysis because the clustered fraction is not defined in such cases. Doing so does not affect the analysed quantity.

We see that the clustered fraction in tabGAP follows similar behaviour to that obtained with both EAM potentials. However, the clustered fraction for interstitials in W-Mo by tabGAP is somewhat lower compared to the W-Mo-EAM potential. In pure W, the interstitial clustered fraction is quite similar for the EAMs and tabGAP, given the standard errors, whilst GAP resulted in more efficient clustering of interstitials.

In the case of vacancies, tabGAP predicted similar clustering in both W and W-Mo as GAP, with the only noticeable difference between the results being at 5 keV.

In general, we note that the tabGAP prediction of the interstitial clustering is less consistent with that of GAP, at least, within the statistical uncertainty available in the present work. This can be explained by the smaller training dataset for the W-Mo pair within the 5-element tabGAP potential.

The results of tabGAP imply that interstitials in W have a substantially higher tendency to form clusters than in W-Mo. Surprisingly, both W-Mo-EAM and GAP predict a rather similar tendency for clustering, although, in all three potentials, we see that the interstitials in W cluster more efficiently than in W-Mo. This is reasonable, given that interstitials are more mobile in W, and can therefore form clusters more swiftly than in W-Mo. In the case of vacancies, only tabGAP and GAP reliably predict that vacancies are less clustered in W, as discussed above.

### C. Dislocations

The energetically most stable dislocation loops in W are those with Burgers vectors of  $1/2 \langle 111 \rangle$  [37, 38]. In all W-Mo cascades, there were only three cases, of dislocations identified by the DXA algorithm in OVITO, whereas pure W only had one case in an AT-ZN EAM simulation. These dislocations were small loops of the interstitial type, formed in the 10- and 20-keV cascades (10 keV in the case of W). The observed dislocations were all  $1/2 \langle 111 \rangle$ , as shown in Fig. 8.

### D. Performance

It is imperative to discuss the difference in performance between the potentials since it was the motivation for developing tabGAP. For example, 100-ps, 5-keV tabGAP simulations using 12 processing cores were completed in less than a day, whereas GAP required a run-time of three days to attain 70 ps simulated time using 1 000 cores.

1 keV simulations (31 250 atoms) using GAP and 192 processor cores ran for 87.7 h on average, which implies that it took around 57.7 ms to compute the equation of motion (EoM) of a single atom per core (performance). The same simulation using tabGAP ran for 2.08 h using 64 cores, so computing the EoM of a single atom took 0.456 ms, which is about 126 times faster than GAP. The EAM potentials, though run on different hardware, were roughly two orders of magnitude faster than tabGAP.

It is worth noting that the tabGAP framework has been further developed after the present simulations using tabGAP had been performed. The new version developed in Ref. [13] has optimised cutoff radii and includes an EAM-like energy contribution, which makes it both more accurate and about 4 times faster than the tabGAP used in the present study.

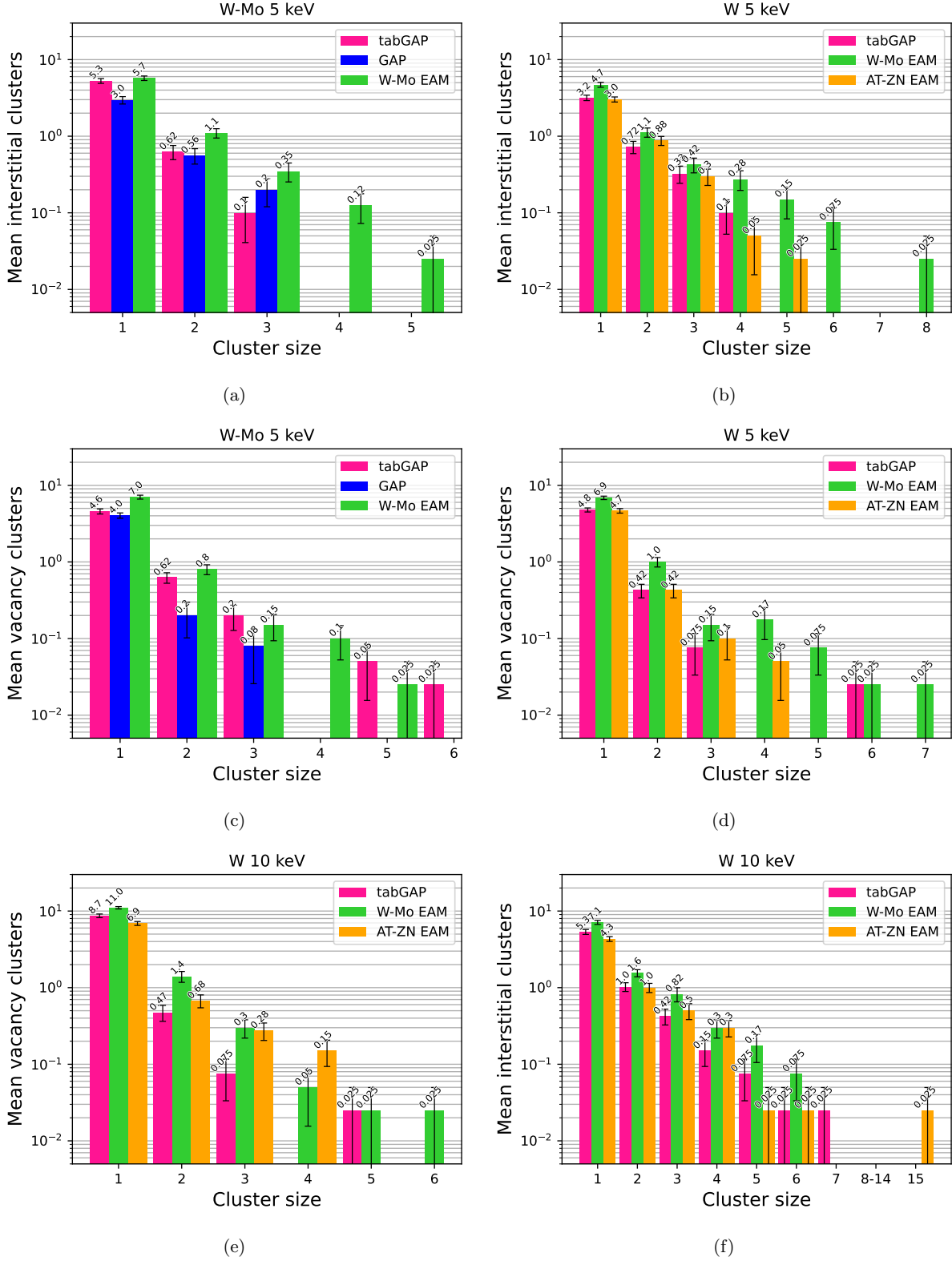


FIG. 6: Histograms of defect cluster size distributions. W-Mo EAM refers to the EAM made for W-Mo. The y-axis is the number of clusters, the x-axis is the cluster size. The numbers atop the bars express their y-values and have been included for clarity due to the usage of a logarithmically scaled y-axis. The vertical line at each bar gives the corresponding standard error (standard errors lower on the y-axis appear significantly larger due to the logarithmic y-axis).

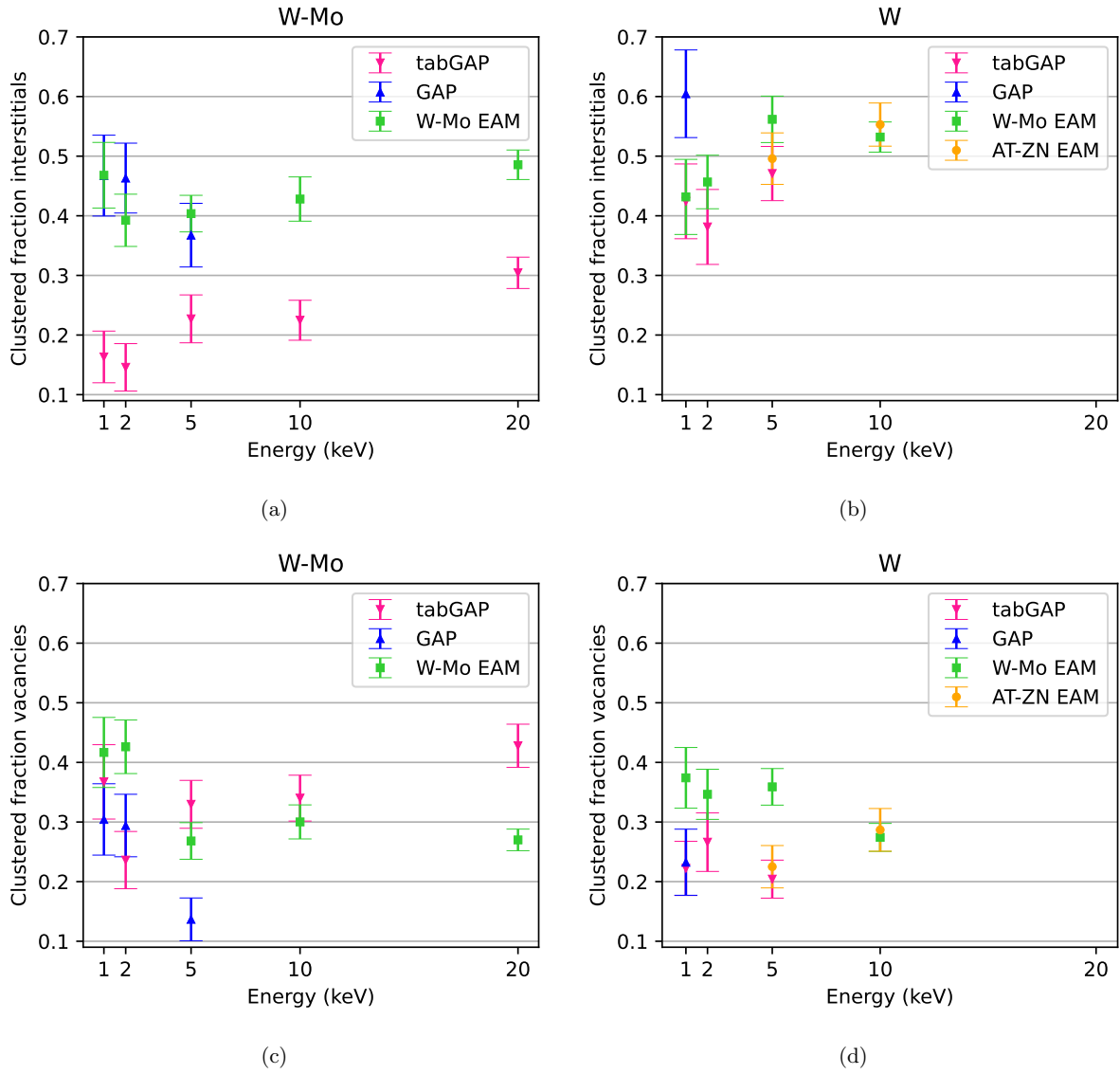


FIG. 7: Clustered fraction of defects. The clustered fraction is computed as shown in Eq. 1. Due to the clustered fraction not being defined for simulations with zero defects, only the simulations with non-zero defects are included in the standard error. The vertical lines indicate the standard error.

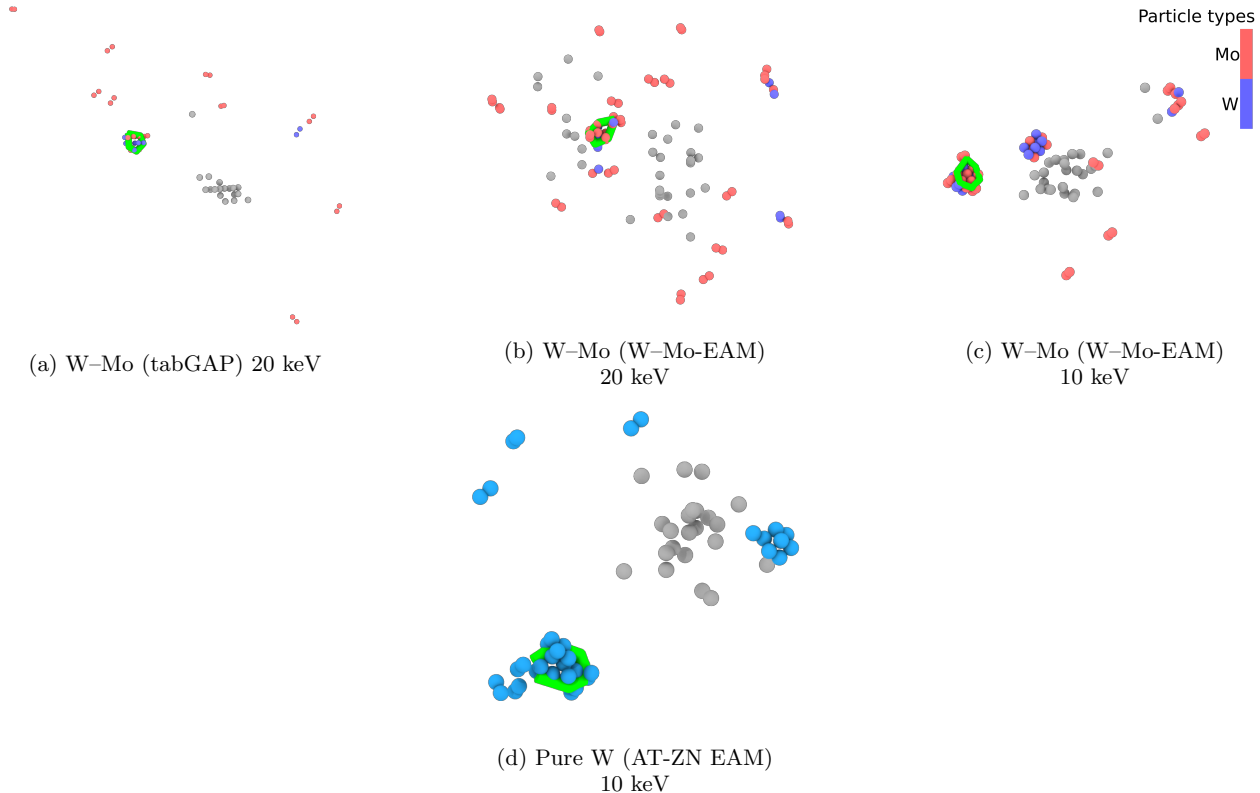


FIG. 8: Defects at the end of the simulations. The grey particles are vacancies, the coloured particles are interstitials (Mo is red, W is blue), and  $1/2 \langle 111 \rangle$  interstitial loops are shown as green lines.

#### IV. SUMMARY OF OBSERVATIONS

For clarity, we here summarise the observations discussed in the previous sections. The comparison between tabGAP and GAP can be summarised as follows:

1. TabGAP was found to be two orders of magnitude faster than GAP, and two orders of magnitude slower than the EAM potentials.
2. The number of surviving Frenkel pairs in tabGAP was found to be close to GAP, albeit always slightly higher, within the uncertainties given by the standard error of the mean.
3. TabGAP and GAP produced similar defect-clustering, within the standard error bars, although there is some difference in the number of specific cluster sizes between the two potentials.
4. We also found that, overall, the fraction of interstitial atoms bound into clusters was smaller in tabGAP than in GAP. The cause for this discrepancy may lie in the smaller training data for tabGAP.

The differences between 50-50 W-Mo alloy and pure W in the primary radiation damage can be summarised as:

1. Interstitials at a given temperature in W-Mo were found to be substantially less mobile than in W.

2. All interstitials in W-Mo and W were split-interstitials.
3. Mo-Mo interstitials were the predominant interstitials in W-Mo.
4. Interstitial clusters in W were larger than in W-Mo. This is likely a result of the superior mobility of interstitials in W allowing for more rapid clustering, as opposed to W-Mo.
5. Small vacancy clusters in W-Mo were found to be more abundant than in W, according to tabGAP and GAP, whereas the W-Mo-EAM did not predict such a difference. This is an expected difference since it is known that EAM potentials generally underestimate the instability of small vacancy clusters in W [9, 35], which is also confirmed by the AT-ZN EAM results, which showed more efficient vacancy clustering than tabGAP.
6. The 50-50 W-Mo had on average the same number of defects as pure W, which implies that the presence of Mo has no significant effect on the cascade dynamics.
7. However, we noticed slightly more efficient recombination of defects in the 50-50 W-Mo alloy, since there were several cases where the defects created in cascades fully recombined. This behaviour was

not observed in pure W. Additionally, W-Mo was observed to recombine a greater fraction of defects produced during the early phase of the cascades.

## V. CONCLUSIONS

The aim of this study was to analyse the benefits and possible drawbacks of a more efficient version of the machine-learning potential GAP, the so-called tabGAP. In this study, we report the differences and similarities between pure W, and W-Mo (50:50) alloy with respect to the primary radiation damage as predicted by three potentials: tabGAP, GAP, and EAM. In W-Mo, the main difference between EAM and (tab)GAP is the number of surviving defects, which is significantly higher in the EAM potential. However, in pure W, the well-established AT-ZN EAM potential produces similar numbers of defects and clustering statistics to tabGAP, which are also fairly similar to the available predictions made by GAP and much lower than the values predicted by the W-Mo-EAM potential.

We conclude that, overall, tabGAP produces similar

results to GAP in cascade simulations in a random binary alloy, while being two orders of magnitude faster. This makes tabGAP a promising machine-learned potential for accurate modelling of low- and high-dose radiation damage in multicomponent alloys.

## VI. ACKNOWLEDGEMENTS

We are grateful for funding from the Academy of Finland project HEADFORE (grant no. 333225). This work has been partly carried out within the framework of the EUROfusion Consortium, funded by the European Union via the Euratom Research and Training Programme (Grant Agreement No 101052200 — EUROfusion). Views and opinions expressed are however those of the author(s) only and do not necessarily reflect those of the European Union or the European Commission. Neither the European Union nor the European Commission can be held responsible for them. The authors wish to thank the Finnish Grid and Cloud Infrastructure (FGCI) (persistent identifier urn:nbn:fi:research-infras-2016072533) for supporting this project with computational and data storage resources.

- 
- [1] S. Zinkle and L. Snead, Designing Radiation Resistance in Materials for Fusion Energy, *Annu. Rev. Mater. Res.* **44**, 241 (2014).
- [2] O. El-Atwani, N. Li, M. Li, A. Devaraj, J. K. S. Baldwin, M. M. Schneider, D. Sobieraj, J. S. Wróbel, D. Nguyen-Manh, S. A. Maloy, and E. Martinez, Outstanding radiation resistance of tungsten-based high-entropy alloys, *Science Advances* **5**, eaav2002 (2019), <https://www.science.org/doi/pdf/10.1126/sciadv.aav2002>.
- [3] M. P. Allen and D. J. Tildesley, *Computer Simulation of Liquids* (Oxford University Press, Oxford, England, 1989).
- [4] K. Nordlund, S. J. Zinkle, A. E. Sand, F. Granberg, R. S. Averback, R. Stoller, T. Suzudo, L. Malerba, F. Banhart, W. J. Weber, F. Willaime, S. Dudarev, and D. Simeone, Primary radiation damage: a review of current understanding and models, *J. Nucl. Mater.* **512**, 450 (2018).
- [5] R. Qiu, Y. Chen, L. Liu, Z. Liu, N. Gao, W. Hu, and H. Deng, Molecular dynamics simulation of primary radiation damage in W-Ta alloys: Effect of tantalum, *Journal of Nuclear Materials* **556**, 153162 (2021).
- [6] H. Li, L. Zhao, Yang Yang, H. Zong, and X. Ding, Improving radiation-tolerance of bcc multi-principal element alloys by tailoring compositional heterogeneities, *Journal of Nuclear Materials* **555**, 153140 (2021).
- [7] A. P. Bartók, M. C. Payne, R. Kondor, and G. Csányi, Gaussian Approximation Potentials: The Accuracy of Quantum Mechanics, without the Electrons, *Phys. Rev. Lett.* **104**, 136403 (2010).
- [8] J. Behler and M. Parrinello, Generalized Neural-Network Representation of High-Dimensional Potential-Energy Surfaces, *Phys. Rev. Lett.* **98**, 10.1103/PhysRevLett.98.146401 (2007).
- [9] J. Byggmästar, A. Hamedani, K. Nordlund, and F. Djurabekova, Machine-learning interatomic potential for radiation damage and defects in tungsten, *Phys. Rev. B* **100**, 144105 (2019).
- [10] G. Sivaraman, A. N. Krishnamoorthy, M. Baur, C. Holm, M. Stan, G. Csányi, C. Benmore, and Á. Vázquez-Mayagoitia, Machine-learned interatomic potentials by active learning: amorphous and liquid hafnium dioxide, *npj Computational Materials* **6**, 104 (2020).
- [11] S. Tovey, A. Narayanan Krishnamoorthy, G. Sivaraman, J. Guo, C. Benmore, A. Heuer, and C. Holm, DFT Accurate Interatomic Potential for Molten NaCl from machine learning, *The Journal of Physical Chemistry C* **124**, 25760 (2020), <https://doi.org/10.1021/acs.jpcc.0c08870>.
- [12] J. Byggmästar, K. Nordlund, and F. Djurabekova, Modeling refractory high-entropy alloys with efficient machine-learned interatomic potentials: Defects and segregation, *Phys. Rev. B* **104**, 104101 (2021).
- [13] J. Byggmästar, K. Nordlund, and F. Djurabekova, Simple machine-learned interatomic potentials for complex alloys, *ArXiv:220308458 Cond-Mat Physicsphysics* (2022), arXiv:2203.08458 [cond-mat, physics:physics].
- [14] A. P. Bartók, R. Kondor, and G. Csányi, On representing chemical environments, *Phys. Rev. B* **87**, 184115 (2013).
- [15] G. Nikoulis, J. Byggmästar, J. Kioseoglou, K. Nordlund, and F. Djurabekova, Machine-learning interatomic potential for W-Mo alloys, *Journal of Physics: Condensed Matter* **33**, 315403 (2021).
- [16] Y. Chen, X. Liao, N. Gao, W. Hu, F. Gao, and H. Deng, Interatomic potentials of W-V and W-Mo binary systems for point defects studies, *Journal of Nuclear Materials* **531**, 152020 (2020).
- [17] S. Plimpton, Fast parallel algorithms for short-range molecular dynamics, *Journal of Computational Physics* **117**, 1 (1995).

- [18] A. Stukowski, Visualization and analysis of atomistic simulation data with OVITO-the Open Visualization Tool, *MODELLING AND SIMULATION IN MATERIALS SCIENCE AND ENGINEERING* **18**, 10.1088/0965-0393/18/1/015012 (2010).
- [19] A. Stukowski, V. V. Bulatov, and A. Arsenlis, Automated identification and indexing of dislocations in crystal interfaces, *Modelling and Simulation in Materials Science and Engineering* **20**, 085007 (2012).
- [20] J. D. Hunter, Matplotlib: A 2D graphics environment, *Computing in Science & Engineering* **9**, 90 (2007).
- [21] G. J. Ackland and R. Thetford, An improved N-body semi-empirical model for body-centred cubic transition metals, *Philosophical Magazine A* **56**, 15 (1987).
- [22] Y. Zhong, K. Nordlund, M. Ghaly, and R. S. Averback, Defect production in tungsten: A comparison between field-ion microscopy and molecular-dynamics simulations, *Phys. Rev. B* **58**, 2361 (1998).
- [23] A. E. Sand, S. L. Dudarev, and K. Nordlund, High-energy collision cascades in tungsten: Dislocation loops structure and clustering scaling laws, *EPL (Europhysics Letters)* **103**, 46003 (2013).
- [24] F. Granberg, J. Byggmästar, and K. Nordlund, Molecular dynamics simulations of high-dose damage production and defect evolution in tungsten, *Journal of Nuclear Materials* **556**, 153158 (2021).
- [25] J. F. Ziegler, J. P. Biersack, and U. Littmark, *The Stopping and Range of Ions in Matter* (Pergamon, New York, 1985).
- [26] K. Nordlund and R. Averback, Point defect movement and annealing in collision cascades, *Phys. Rev. B* **56**, 2421 (1997).
- [27] W. G. Hoover, Canonical dynamics: Equilibrium phase-space distributions, *Phys. Rev. A* **31**, 1695 (1985).
- [28] S. NOSÉ, A molecular dynamics method for simulations in the canonical ensemble, *Molecular Physics* **100**, 191 (2002), <https://doi.org/10.1080/00268970110089108>.
- [29] K. Nordlund, Molecular dynamics simulation of ion ranges in the 1–100 keV energy range, *Computational Materials Science* **3**, 448 (1995).
- [30] K. Nordlund, S. J. Zinkle, A. E. Sand, F. Granberg, R. S. Averback, R. E. Stoller, T. Suzudo, L. Malerba, F. Banhart, W. J. Weber, F. Willaime, S. L. Dudarev, and D. Simeone, Primary radiation damage: A review of current understanding and models, *Journal of Nuclear Materials* **512**, 450 (2018).
- [31] J. F. Ziegler, SRIM-2013 software package, available online at <http://www.srim.org>.
- [32] J. F. Ziegler, J. P. Biersack, and M. D. Ziegler, *SRIM - The Stopping and Range of Ions in Matter* (SRIM Co., Chester, Maryland, USA, 2008).
- [33] J. Lindhard, M. Scharff, and H. E. Schiøtt, Range concepts and heavy ion ranges, *Kgl. Danske Vid. Selskab, Mat.- Fys. Medd.* **33** (14), 1 (1963).
- [34] J. Byggmästar, F. Granberg, and K. Nordlund, Effects of the short-range repulsive potential on cascade damage in iron, *Journal of Nuclear Materials* **508**, 530 (2018).
- [35] D. R. Mason, D. Nguyen-Manh, M.-C. Marinica, R. Alexander, A. E. Sand, and S. L. Dudarev, Relaxation volumes of microscopic and mesoscopic irradiation-induced defects in tungsten, *Journal of Applied Physics* **126**, 075112 (2019), <https://doi.org/10.1063/1.5094852>.
- [36] J. Byggmästar, K. Nordlund, and F. Djurabekova, Gaussian approximation potentials for body-centered-cubic transition metals, *Phys. Rev. Materials* **4**, 093802 (2020).
- [37] S. Hasanzadeh, R. Schäublin, B. Décamps, V. Rousson, E. Autissier, M. Barthe, and C. Hébert, Three-dimensional scanning transmission electron microscopy of dislocation loops in tungsten, *Micron* **113**, 24 (2018).
- [38] P.-W. Ma, D. R. Mason, and S. L. Dudarev, Multi-scale analysis of dislocation loops and voids in tungsten, *Phys. Rev. Materials* **4**, 103609 (2020).

## VII. APPENDIX

### A. Time-integration error

Here we compare the time-integration error between the three potentials. To test this, we ran test simulations, using the velocity Verlet algorithm, in cells comprising 1 024 atoms, that were not connected to thermostats or barostats, making them *NVE* ensembles; ensembles where the total energy should stay constant. In Fig. 9, one can see the results from simulations for all of the potentials for varying values of time step, using the aforementioned cell at a temperature of 500 K; the flatter the line, the better. Fluctuations of total energy in an *NVE* ensemble are due to time-integration error, caused by having a non-zero time step.

Interestingly, tabGAP shows erratic variation in total energy (Fig. 9a), whereas EAM and GAP show more consistency in the pattern of the variation. The erratic variation of tabGAP could be caused by interpolation error. Even so, the largest fluctuation per atom (5 – fs time step) is only  $\approx 0.15$  meV, whereas for GAP and EAM respectively, these are  $\approx 0.06$  meV and  $\approx 0.08$  meV. The average kinetic energy of an atom in these simulation is  $\frac{3}{2} k_B 500 \text{ K} \approx 65$  meV. Therefore, changes in the energy of an atom caused by tabGAP are completely masked by thermal vibrations and are thus insignificant.

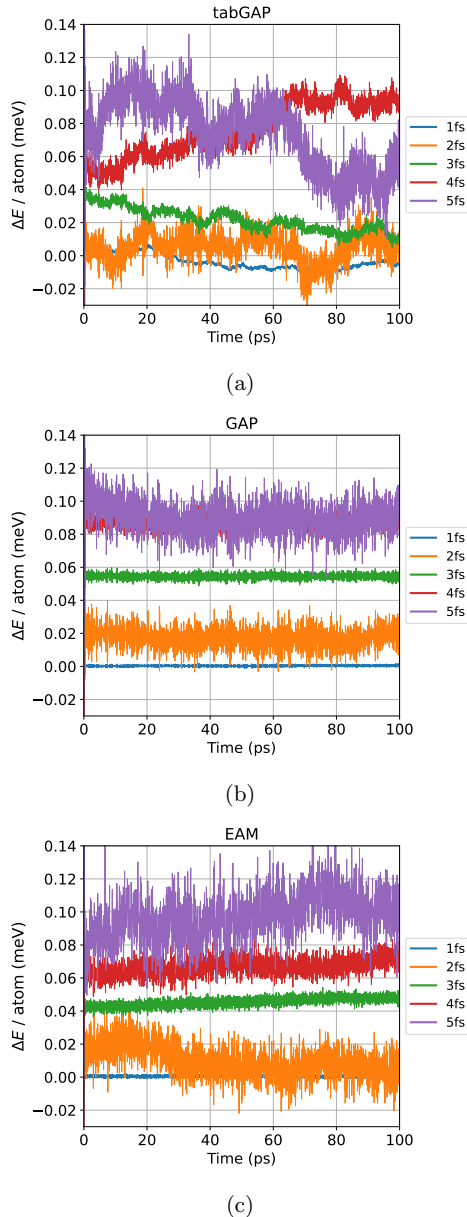


FIG. 9: The y-axis shows total-energy variations per atom in a W-Mo *NVE* ensemble of 1 024 atoms. The y-axis values have been shifted for clarity, but the magnitudes of relative changes therein are unchanged. The energy variations are computed by subtracting each energy value from a fixed value and dividing it by the number of atoms in the cell.

# Supplementary information for: Efficient atomistic simulations of radiation damage in W and W-Mo using machine-learning potentials

Mikko Koskenniemi,<sup>1,\*</sup> Jesper Byggmästar,<sup>1</sup> Kai Nordlund,<sup>1</sup> and Flyura Djurabekova<sup>1,2</sup>

<sup>1</sup>*Department of Physics, P.O. Box 43, FI-00014 University of Helsinki, Finland*

<sup>2</sup>*Helsinki Institute of Physics, Helsinki, Finland*

(Dated: August 2, 2022)

Figure 1 shows defect clusters for W-Mo and W in the 1-2 keV range, and Figure 2 contains the 10-20 keV plots for W-Mo.

arXiv:2208.00804v1 [cond-mat.mtrl-sci] 1 Aug 2022

---

\* Corresponding author, mikko.a.koskenniemi@gmail.com

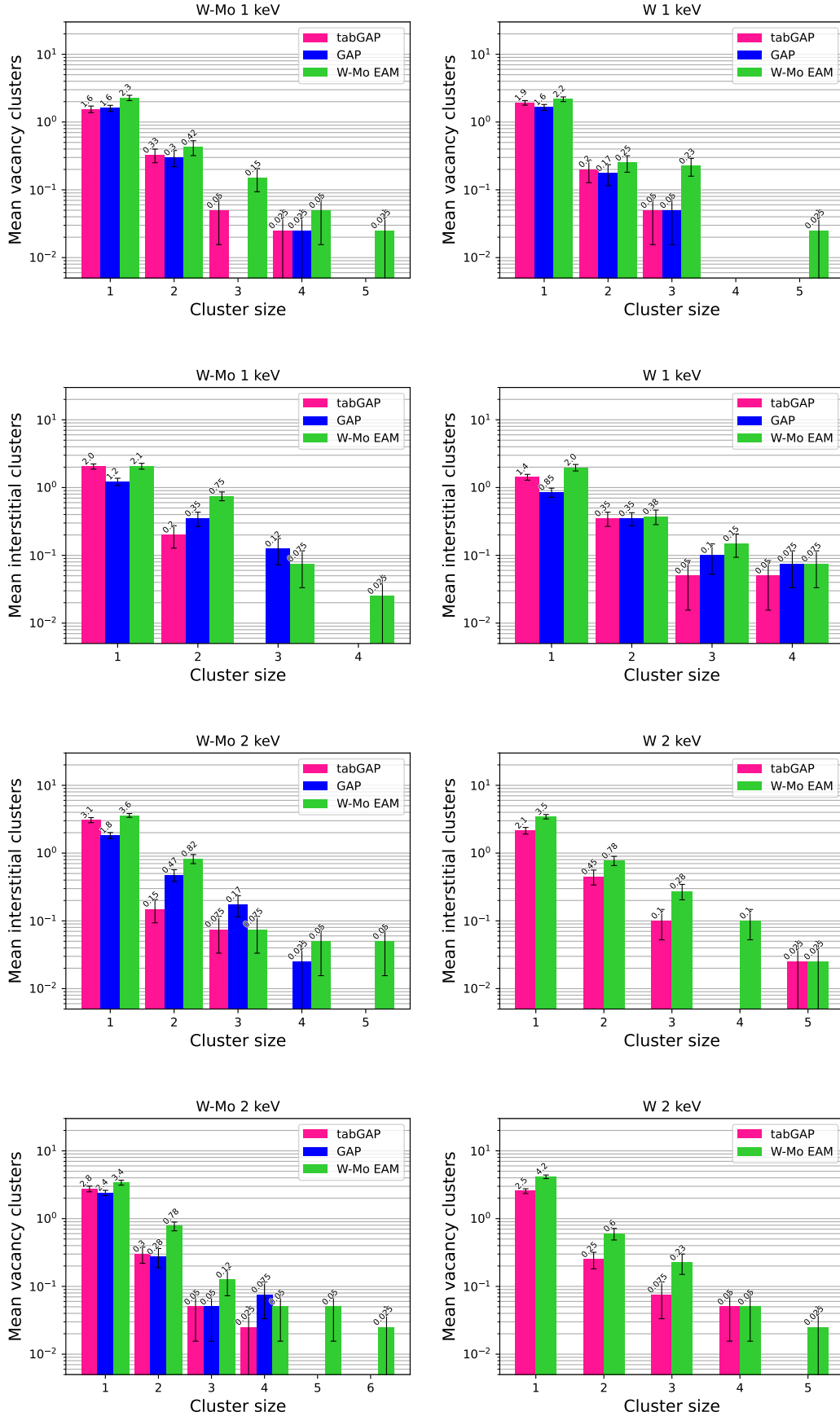


FIG. 1: The rest of the defect-cluster plots comparing W-Mo and W. The numbers atop the bars express their y-values. The vertical line at each bar gives their standard error (standard errors lower on the y-axis appear larger due to the logarithmic y-axis).

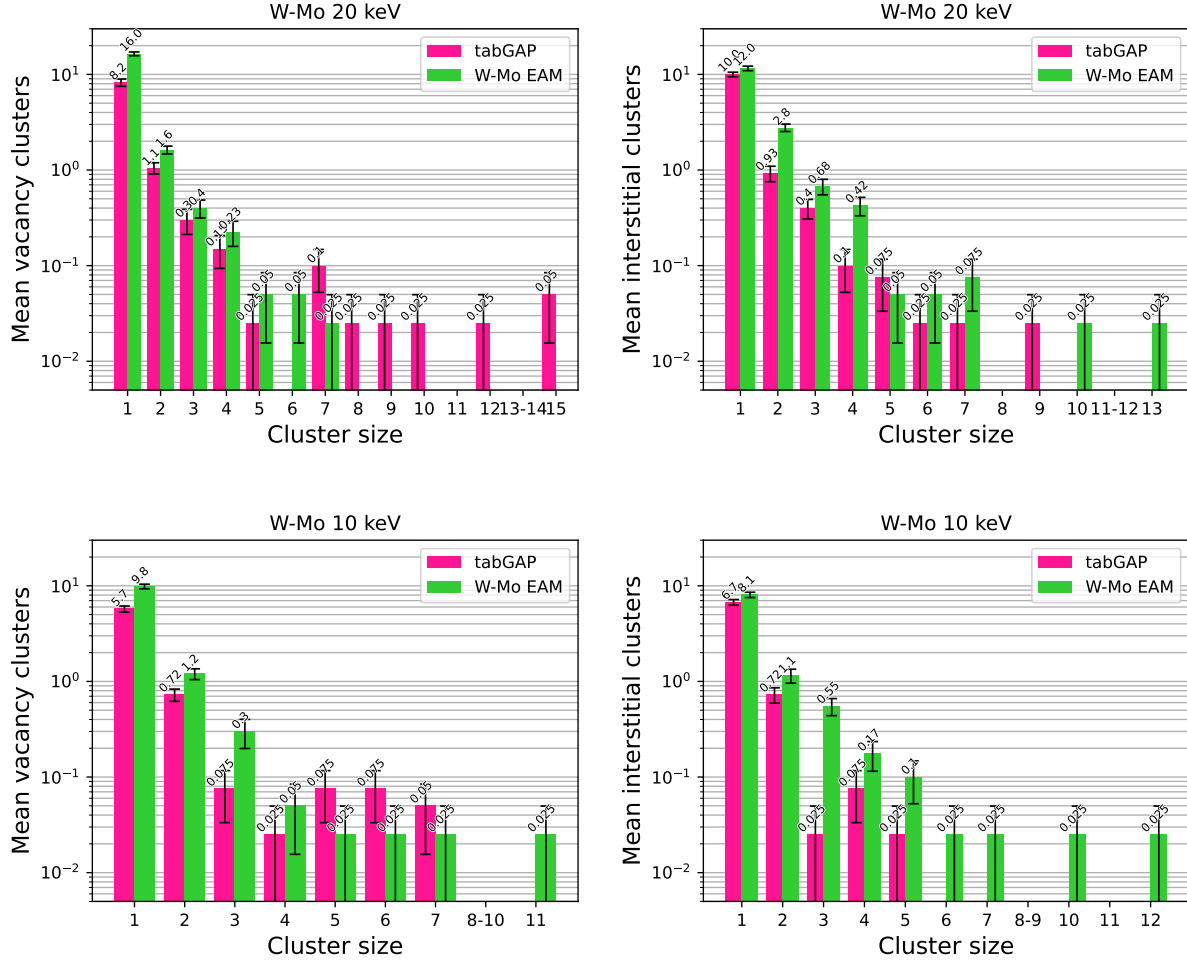


FIG. 2: The rest of the defect-cluster plots. The numbers atop the bars express their y-values. The vertical line at each bar gives their standard error (standard errors lower on the y-axis appear larger due to the logarithmic y-axis).